RSC Advances

PAPER

View Article Online
View Journal | View Issue

Cite this: *RSC Adv.*, 2026, **16**, 4993

Hollow zinc phthalocyanine nanoshells: quick low temperature synthesis, enhanced near-IR absorption and water-dispersibility for photocatalysis and phototherapy

Shweta Sharma and Amiya Priyam *

Received 24th September 2025
Accepted 16th January 2026

DOI: 10.1039/d5ra07242e

rsc.li/rsc-advances

A quick (two minutes), low temperature (10 °C) synthesis has been developed to obtain crystalline and hollow zinc phthalocyanine (ZnPc) nanoshells (major axis: 32.0 ± 5.2 nm, aspect ratio: 1.3, void size: 18.1 ± 2.3 nm) with a redshift of the Q-band and emergence of a new NIR peak (746 nm). Thioglycolic acid (TGA)-capping uniquely imparts the ability for it to act as solo photocatalyst which was not found in uncapped ZnPc NPs. In addition, it also exhibited robust photothermal effect (ΔT = 16 °C) under NIR-LED (660 nm) irradiation. The optimum sub-50 nm size also makes them well suited for phototherapy as well.

Zinc-phthalocyanine (ZnPc) is a photosensitizer (PS) drug approved by the FDA for photodynamic therapy (PDT)[1] having a diamagnetic centre that enhances the generation of $^1O_2$ species.[2] Moreover, ZnPc has a large absorption cross-section of light at the tissue-penetrating spectral range of 650–900 nm.[3] However, due to its high hydrophobic nature, it exhibits poor solubility in water or body fluids, low physiological acceptability and therefore it is difficult to administer directly to cancer patients.

In addition to therapeutics, ZnPc also plays key role in photocatalytic applications. Some of the well-known semiconductor photocatalysts such as TiO_2, ZnO, MgO *etc.* absorb in the UV region which constitutes only 5% of the solar spectrum. The conjugation of such materials with ZnPc imparts light-harvesting ability in the vis-NIR range and enhances the photocatalytic efficiency in sunlight.[4,5] The process involves excitation of ZnPc in sunlight which leads to injection of electrons into the conduction band of semiconductors and the photocatalysis ensues. Similar enhancement in photocatalytic efficiency has also been reported in metal-ZnPc conjugates.[6,7] While there are numerous reports of such metal- or semiconductor-ZnPc conjugates as catalysts, the works on ZnPc as a solo photocatalyst are scarce. For a cost-effective, efficient and sustainable photocatalysis methodology, it is essential to develop modified ZnPc variants that have good water-dispersibility. Waste water purification, water-splitting reactions and RAFT (reversible-addition-fragmentation chain transfer) polymerizations[8–10] are such crucial areas which require good dispersibility of catalysts in aqueous medium.

To overcome the limitations, several chemical and physical modifications have been employed such as sulfonation, PEGylation, quaternization and encapsulation.[11,12] For example, ZnPc derivatives, such as sulfonated ZnPc have been designed to increase the water solubility.[13,14] However, these processes require multiple and complex chemical functionalization steps, during which the photoactivity could be reduced by destroying the original electronic conjugation system of the photosensitizer. With the advent of nanotechnology, new strategies have evolved which utilize the π–π interaction between the rings and the ZnPc molecules have been self-assembled into various types of nanostructures.[14–17] Moon *et al.*[14] developed a vaporization–condensation–recrystallization (VCR) method to make crystalline ZnPc nanowires (length: 1–10 μm; diameter: 50–100 nm) by vaporizing ZnPc powder (PW) at 550 °C followed by condensation. ZnPc nanoparticles (NPs) were also prepared by using concentrated sulfuric acid, CTAB solution and annealing at 200 °C.[17] However, the NPs were amorphous and lacked crystallinity. Wang *et al.*[16] prepared spherical ZnPc NPs by adding ZnPc and DMSO dropwise to water with 4 hours of stirring and subsequent dialysis. In a pioneering approach, hollow ZnPc nanospheres comprising of covalently linked Pc units were synthesized which showed better singlet oxygen efficiency, however, they were amorphous and much bigger, about 230 nm in diameter.[18] For an efficient cell-internalization process, ideal size range has been estimated to be 25–50 nm.[19]

As mentioned above, harsh physicochemical conditions and lengthy procedures were necessitated for making ZnPc dispersible in water either through chemical modifications or by making nanoparticles. In contrast, through this work, we

Department of Chemistry, School of Physical and Chemical Sciences, Central University of South Bihar, NH-120, Gaya-Panchanpur Road, Gaya-824236, India. E-mail: apriyam@cub.ac.in

report a novel form of ZnPc, a crystalline hollow nanoshells within sub-50 nm size regime. These nanoshells are highly water-dispersible due to surface capping of thioglycolic acid (TGA) and can also be obtained in the form of re-dispersible nano-powders (SI, Sections, S1.1–S1.3). The methodology as shown in Fig. 1a is quicker, cleaner and greener as the entire synthesis is performed in aqueous medium at a low temperature of 10 °C under ultrasonication for 2 minutes. The TGA-capped HZPNS *i.e.*, HZPNS@TGA also exhibits a further red-shifted peak to the NIR region. The water-dispersibility, NIR tunability and ideal size regime makes it suitable for light-induced therapeutic applications such as PDT and photothermal therapy (PTT). The thiol-capping also enhances its photocatalytic activity which is vividly shown in the work.

Fig. 1b shows the optical properties of the ZnPc. B-band (peaks ranging from 332 to 391 nm) and Q-band (peaks ranging from 609 to 775 nm) can be clearly seen for the samples under study. These are attributed to π–π* electronic transitions from S_0 to S_2 and S_0 to S_1 states, respectively for B- and Q-bands. In the molecular state, two peaks appear in the Q band, at 609 and 671 nm. When these planar rings of ZnPc molecules are stacked in a particular order, nanoparticles are formed. Following the scheme given in Fig. 1a, TGA-capped ZnPc nanoshells as well as bare (uncapped) ZnPc nanoparticles were prepared. The Q-band of nanoparticles showed a remarkable red-shift in the following manner: 671 nm (molecular state) → 678 nm (uncapped NPs) → 684 nm (TGA-capped nanoshells) → 775 nm (bulk state). As compared to bulk ZnPc semiconductor, the bare NPs and TGA-capped HZPNS exhibit a huge blue shift of 97 nm and 91 nm, respectively. These spectral shifts suggest a slipped cofacial orientation in the solid state.[20] Furthermore, the band gap for the bulk ZnPc semiconductor was found to be 1.49 eV which blue-shifted to 1.58 eV and 1.75 eV for the hollow nanoshells and bare nanoparticles, respectively. This is attributed to the quantum confinement of charge carriers.[21] The energy gaps for the Q-band were calculated from the first point of inflection from the lower energy side in the first derivative absorption spectra. In contrast, previous researchers found no red shift in ZnPc nanoshells,[18] which were bigger than 200 nm and were formed due to covalent linkage of ZnPc rings through side arms. Some other forms such as nanowires[14,15] show some redshift of the peak but were much bigger in size (length: 1–10 μm, and diameter: 50–100 nm).

In addition, uniqueness of TGA-capped HZPNS is underscored as it exhibits a new peak at 746 nm within the Q-band in the near IR region, which arises from π–π interactions and binding of thiol group. As can be seen from the Gaussian deconvolutions (Fig. S1), this NIR peak contributes substantially ~38% to the overall intensity of Q-band. As seen in Fig. 1, B-band shows a significant blueshift of 59 nm on moving from bulk ZnPc semiconductor (391 nm) to TGA-capped hollow nanoshells (332 nm). It suggests that the nature of π–π interactions are quite different in nanocrystals as compared to bulk semiconductor. The photoluminescence (PL) spectra (Fig. S3) of all the samples were also recorded at two different excitation wavelengths, 350 nm and 600 nm. As compared to molecular state, the PL spectra was substantially quenched in both the spectral regions, 360–600 nm and 620–800 nm, for the nanoparticles, nanoshells and the bulk. It implies that the energy dissipation in ZnPc nanocrystals proceeds in non-radiative manner through lattice vibrations.[20]

The HRTEM image in Fig. 2a clearly illustrates the highly crystalline nature of the nanoparticles. Additionally, it also

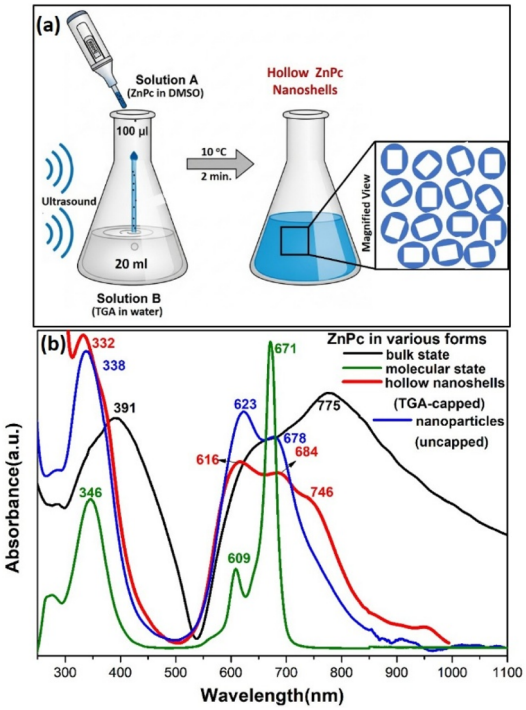

Fig. 1 (a) Scheme representing ultrasonic synthesis of hollow ZnPc nanoshells with surface-capping of thioglycolic acid (TGA) at 10 °C under two minutes of ultrasonic irradiation [Solution A: 10 mM ZnPc in DMSO; Solution B: 1.4 mM TGA in deionized water; ultrasound frequency: 40 kHz, ultrasound power: 100 W]. (b) UV-vis-NIR absorption spectra of Zinc Phthalocyanine (ZnPc) in various forms.

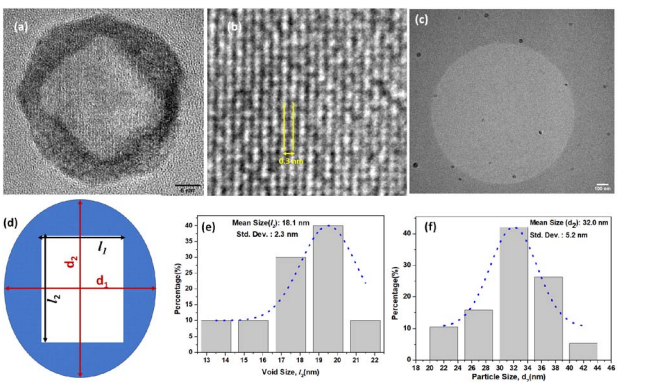

Fig. 2 (a) HR-TEM image of TGA capped hollow ZnPc nanoshells (HZPNS), (b) zoomed-in view showing lattice fringes, (c) low magnification TEM image showing particle size and shape distribution. (d) Schematic view of the nanoshell defining the lengths along different axes, (e) histogram showing distribution of void size (l_2) in HZPNS and (f) histogram showing distribution of diameter (d_2) along major axis in HZPNS.

shows that the nanocrystals have ellipsoid shape with rectangular void space. Fig. 2b shows the magnified view wherein interplanar spacing of 0.3 nm can be seen. Low magnification image is shown in Fig. 2c which illustrates the size and shape distribution profile of the nanoparticles. Fig. 2d shows the schematic description of the hollow nanoshells.

Further, crystallinity of the samples were analysed by X-ray diffraction. The XRD patterns of the nanopowders of TGA-capped HZPNS is displayed in Fig. 3a. Intense peaks can be seen at the 2θ values of 6.8, 8.9, 18.0, 27.8, 29.0, 32.3 and 33.7° which correspond to interplanar spacing (d-values) of 12.9, 9.9, 4.9, 3.2, 3.0, 2.7 and 2.6 Å, respectively. Several peaks such as 6.8, 8.9, 18.0, 26.2, and 27.8° match very well with the β-phase of the bulk ZnPc (Fig. 3b) that are attributed to lattice planes with hkl values of −101, 101 and −301, 311 and −305, respectively [JCPDS card no. 39-1882]. However, the maximum intensity is observed for the reflections at 29.0° (d-spacing: 3.0 Å) followed by 33.7° line. It indicates a different crystal packing pattern due to binding of thioglycolic acid to Zn-site in the nanoshells. It is in good agreement with the interplanar spacing determined through HRTEM imaging (Fig. 2b). Similar high intense lines in the 28–45° region was also observed by earlier workers for ZnPc modified with eight carboxyl groups.[22,23] The width of the most intense XRD peak at 29° was further analysed by Debye–Scherrer equation and the average crystallite size was found to be 32.4 nm, which corroborates the size determined by HR-TEM. Furthermore, on TGA binding, the change in crystal packing pattern also underscores a change in π–π interaction that correlates well with the emergence of a new peak at 746 nm in the optical absorption spectra (Fig. 1b).

In the absence of TGA capping agent, the as-prepared ZnPc NPs appear to be aggregated as shown in the TEM images (Fig. S2). These bare ZnPc NPs have ellipsoid-like shape with average mean diameter, d_1 (minor axis), of 57.4 ± 10.9 nm (Fig. S2b) and average aspect ratio (d_2/d_1) of 1.32 ± 0.11 (Fig. S2c). Thus, TGA not only reduces the size, it also improves the crystallinity and homogeneity. In addition, internal void space is also created under identical conditions of ultrasound irradiation and temperature. The unique structure-directing ability of TGA is thus underscored. Mechanistically, the synthesis under ultrasound irradiation involves 'acoustic cavitation' phenomenon, in which a bubble is formed, grows in size and then collapses.[24] It has been shown earlier that ultrasound activates the reorientation and adsorption of thiol surfactants[25] thereby enhancing their self-assembly. During the interfacial assembly, chemical precursors or pre-formed thiol-capped subnanoclusters are likely driven to the surface of the bubble (the gas–liquid interface) by the high-speed microstreaming forces. The heat from the bubble's collapse cross-links the material at the interface, forming a solid shell leaving a void space within.[26]

The binding of TGA to the particle surface has been investigated by Raman spectroscopy as shown in Fig. 4. Raman spectra in the lower frequency regime are shown for both the samples, bulk ZnPc (Fig. 4a) and the TGA-capped nanoshells (Fig. 4b). When the synthesis is carried out in presence of TGA, a new peak appears at 225 cm^{-1} which is attributed to Zn–S(thiol) stretching vibrations.[27–29] At 430 cm^{-1} coupled mode of Zn–S(thiol) is also observed. In addition, the peaks at 623 and 700 cm^{-1} are assigned to C–S stretching vibrations, related to gauche and trans conformations, respectively. Thus, Raman spectroscopy provides crucial evidence of thiol-capping of the surface of ZnPc nanoshells.

The FTIR spectra (Fig. 5) further support the findings of Raman spectroscopy. The negative peaks at ∼1326, 1163, 1113, 1055, 875 and 748 cm^{-1} in ZnPc-bulk powder are assigned to phthalocyanine skeletal vibrations.[30] On nanoparticle formation (TGA-HZPNS and bare ZnPc NPs) from solution phase, the peak at 1055 cm^{-1} is affected in three ways; it shifts to 1059 cm^{-1}, broadens and becomes the most intense vibration. Concomitantly, the peak at 1326 cm^{-1} shows a blueshift of 6 cm^{-1} and moves to 1332 cm^{-1} in both the nanophase materials.

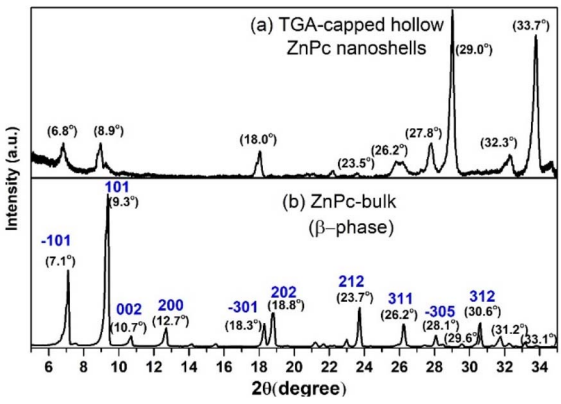

Fig. 3 Powder X-ray diffractograms of (a) TGA-capped hollow ZnPc nanoshells and (b) ZnPc bulk.

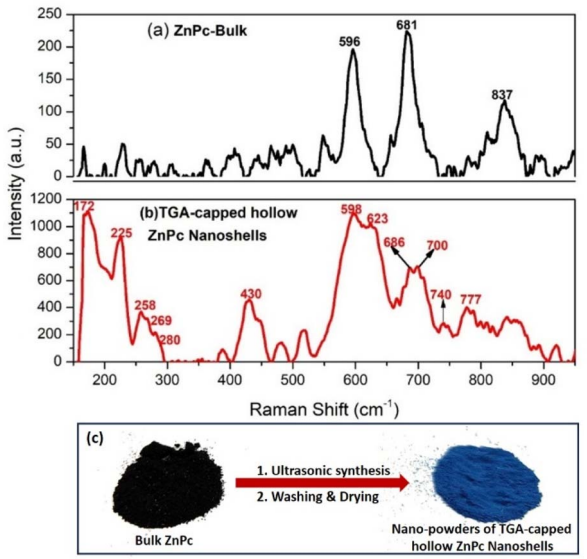

Fig. 4 Raman spectra of (a) bulk ZnPc and (b) TGA-capped hollow ZnPc nanoshells (b). (c) Photograph showing the transformation of bulk ZnPc powders to nanopowders of hollow ZnPc nanoshells (HZPNS).

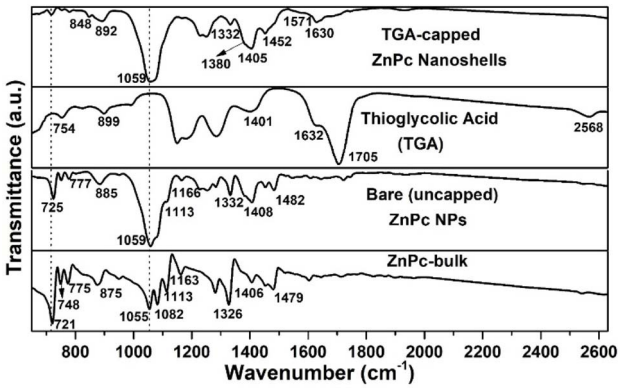

Fig. 5 FTIR spectra in the 650–2600 cm^{-1} region of TGA-capped HZPNS, pristine TGA solution, bare ZnPc NPs and bulk ZnPc. The spectra of 2600–3800 cm^{-1} region is given in Fig. S4, SI.

The three sharp peaks are also observed in ZnPc-bulk sample between 700 and 800 cm^{-1}, at 721, 748 and 775 cm^{-1}. Two of these peaks, at 721 and 775 cm^{-1}, are out-of-plane modes, and the one at 748 cm^{-1} is in-plane mode.[30] The out-of-plane modes are quite sensitive to the crystal structure. Any change in the packing pattern of the 3-D lattice would alter these peaks. The relative intensity of the peaks decreases in bare ZnPc NPs while it is considerably diminished in the TGA-capped HZPNS. In the XRD patterns (Fig. 3), the same was evidenced as a major change in the crystal structure of TGA-capped HZPNS *vis-à-vis* bulk-ZnPc.

In FTIR spectrum of pristine TGA, the S–H stretching can also be seen as a low intensity peak at 2568 cm^{-1}, which disappears as S binds to Zn-site on the hollow nanoshells. The most-intense peak at 1705 cm^{-1} is assigned to C=O stretching vibrations,[31] which disappears implying that the most of free COOH groups on TGA ionize to COO^{-}. The vibrations at 1380 and 1571 cm^{-1} in the hollow ZnPc nanoshells are attributed to the symmetric and asymmetric stretching of COO^{-}, respectively. The peak around 1630 cm^{-1} is present in both the spectra that is assigned to OH bending modes of water bound to TGA molecules. In the high frequency region (Fig. S4), the relative intensity of peaks at 3220 and 3452 cm^{-1} corresponding to OH-stretching[31] decreases considerably on TGA binding to the hollow nanoshells.

As the thiol-end preferentially binds to Zn-sites on the crystal lattice due to its stronger affinity; the carboxy-end remains free which can interact with water molecules thereby greatly enabling and enhancing its dispersibility in aqueous system. As shown in Table S1 and Fig. S5, the zeta potential of bare ZnPc NPs is −3.6 mV which turns more negative, −28.5 mV for TGA-capped HZPNS. The latter acquires substantial surface charge on account of ionization of carboxyl group which imparts a combination of steric and electrostatic stabilization. Moreover, for intravenous administration, a negative surface charge is considered beneficial for long-term drug delivery to solid tumors.[32] There are negatively charged components in extracellular matrix of solid tumours that can easily bind to positively charged NPs thereby severely restricting its diffusion. In contrast, negatively charged NPs exhibit better accumulation and deeper penetration in 3D tumor spheroids.[33]

The colloidal solution of hollow ZnPc nanoshells can also be converted into solid nano-powders, which is possible due to strong binding of TGA to the ZnPc nanoshells. Fig. 4c shows the transformation of bulk ZnPc powders to nanopowders of TGA-capped HZPNS. The sharp colour change from blackish blue to dark blue can easily be discerned. These nanopowders can be easily re-dispersed in water to give a transparent blue solution which regenerates the original absorption spectrum of the colloidal nanoshells.

To check the efficacy of the ZnPc nanoparticles as solo photocatalysts, methyl orange (MO) degradation was chosen as the model system. Photocatalysis (Section S1.5) has been carried out under the ambient light conditions indoors. The thiol-capped ZnPc nanoshells were found to act as a robust photocatalyst for the degradation of MO dye. In contrast, uncapped ZnPc nanoparticles or ZnPc in molecular state do not show any photocatalytic activity. Fig. 6 describes the remediation of MO dye under in-house lighting condition with four white LED bulbs with the power of 9 W each. The decrease in MO absorption was followed which is shown in Fig. 6a. The inset of Fig. 6a shows the plot of $-\ln(A/A_o)$ at a wavelength of 497 nm *versus* irradiation time. The dye degradation followed a first order kinetics and the rate constant was found to be 0.00145 min^{-1}. Another set of dye degradation was attempted with bare or uncapped ZnPc nanoparticles. However, no change in absorption profile of MO dye was observed even after 24 hours of irradiation (Fig. 6b). This clearly confirms that TGA-capping imparts the catalytic activity. Here, we also note that a good catalytic efficiency has been achieved for TGA-capped HZPNS, even without the assistance of additional electron donor species, such as TEOA, isopropanol or semiconductor nanoparticles, which is in contrast to the earlier reports.[34–36]

Mechanistically, singlet oxygen produced on white light irradiation likely brings about oxidative degradation of methyl orange. It is a strong electrophile and the plausible mechanism involves the attack on the electron-rich site such as azo(–N=N–) group,[37] which is also the main chromophore in MO molecule. The reaction may proceed through a series of aromatic intermediates, getting transformed as aliphatic acid such as oxalic acid and finally degraded into CO_2 and H_2O.[38]

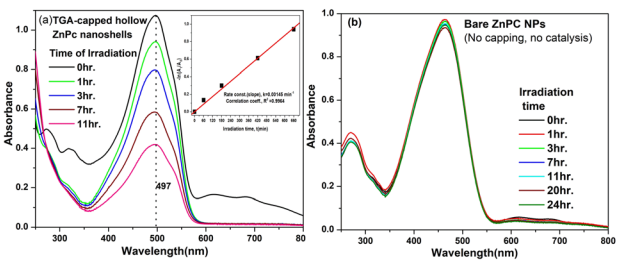

Fig. 6 Degradation of methyl orange (MO) under ambient in-house lighting with four white LED bulbs of 9 W each: (a) absorption of MO recorded at different time intervals in presence of (a) TGA-capped hollow ZnPc nanoshells (HZPNS), and (b) bare ZnPc NPs; (inset) logarithmic plot of absorbance against irradiation time.

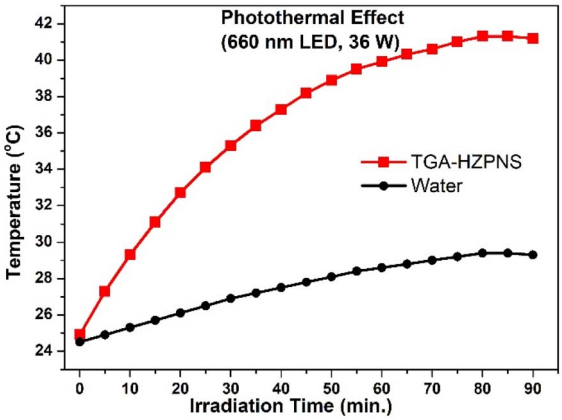

Fig. 7 Photothermal effect as demonstrated through the temperature changes of TGA-capped HZPNS (0.1 mg ml^{-1}) upon NIR irradiation (660 nm, 20 LED pcs, 36 W, 40 mW cm^{-2}).

In addition to robust photocatalytic activity, the TGA-capped HZPNS also exhibit light-induced hyperthermia. In most of the photothermal studies, laser has been employed as the light source due to its high monochromaticity, intensity and coherence.[14] However, it is expensive and difficult to maintain. In contrast, light emitting diode (LED) overcomes these limitations; it has lower cost, longer lifetime and better power conversion efficiency.[39] Herein, photothermal effect has been investigated using an array of 660 nm LEDs with 36 W power (Fig. 7). The solution was irradiated under the LED panel and the temperature rise was monitored by a digital thermometer. As can be seen in the Fig. 7, for the aqueous solution of TGA-HZPNS, the temperature rises exponentially from 25 °C to 41 °C ($\Delta T = 16$ °C) for 90 minutes of irradiation. The control set, consisting of deionized water, shows a much smaller increase of 5 °C under identical condition. This property can be further harnessed to enhance the cancer phototherapy.

In conclusion, thiol-capped, crystalline and hollow ZnPc nanoshells have been prepared for the first time by devising a quicker (2 min), simplified and sustainable method consuming less energy and generating no waste. Unique ability of TGA as a structure directing agent, *i.e.* creating inner void space, has been discovered. Furthermore, TGA has a multiplier effect. Besides, providing stability and water-solubility, it also imparts photocatalytic activity which is the key finding of this work. It unveils the potential of thiol-capped ZnPc NPs to act as a solo catalyst in many other industrially and environmentally relevant reactions. This removes the multitudes of reagents for making a composite-catalyst. TGA-capping extends the absorption further into NIR region, thus a major part of sunlight from visible to NIR can be effectively harvested for various photo-induced processes. Especially, its role as nanomedicine in light-induced therapies gets augmented. The pristine ZnPc molecules are known to exhibit a robust photodynamic effect, however, loading them onto a nano/micro-carrier was necessitated for transportation to the site of action. The TGA-capping eliminates the need for external carriers. The carboxyl end remains free which opens up a window for bioconjugation with antibodies for targeting specific diseases. In addition to PDT effect, the crystalline packing of ZnPc rings also imparts photothermal efficiency which was peculiarly observed under low power LED lights. Thus, when irradiated with NIR light, it will act as dual mode therapeutic tool to hasten the killing of cancerous cells, by twin modalities of photothermal and photodynamic therapies working in tandem. Additionally, with the thiols as capping agent, a third modality "disulfidptosis"[40,41] may also be explored to enhance the overall therapeutic efficacy.

Conflicts of interest

There are no conflicts to declare.

Data availability

Data will be made available on request.

Supplementary information (SI): the suppporting data: S1. Experimental details, S2. Deconvolutions of the Q-band of various forms of ZnPc, S3. TEM images and size distribution histogram of bare ZnPc nanoparticles, S4. Photoluminescence Spectra of ZnPc in various forms, S5. Zeta potential of the ZnPc nanoparticles and nanoshells. See DOI: https://doi.org/10.1039/d5ra07242e.

Acknowledgements

HRTEM images were taken at central research facility (CRF), IIT-ISM, Dhanbad, India.

References

1 L. P. Roguin, N. Chiarante, M. C. García Vior and J. Marino, *Int. J. Biochem. Cell Biol.*, 2019, **114**, 105575.
2 E. Lima and L. V. Reis, *Molecules*, 2023, **28**, 5092.
3 T. Nyokong, *Pure Appl. Chem.*, 2011, **83**, 1763–1779.
4 S. R. D. Gamelas, J. P. C. Tomé, A. C. Tomé and L. M. O. Lourenço, *RSC Adv.*, 2023, **13**, 33957–33993.
5 S. Keshipour and A. Asghari, *Int. J. Hydrogen Energy*, 2022, **47**, 12865–12881.
6 S. Mgidlana, Y. I. Openda and T. Nyokong, *J. Mol. Struct.*, 2023, **1277**, 134850.
7 E. Dube, N. Nwaji, D. O. Oluwole, J. Mack and T. Nyokong, *J. Photochem. Photobiol., A*, 2017, **349**, 148–161.
8 S. Zhang, C. Tian, X. Jiang, X. Xu, H. Zhao, J. Sun, L. Zhang and Z. Cheng, *Eur. Polym. J.*, 2023, **196**, 112313.
9 J. Sun, H. Zhao, S. Zhang, X. Xu, W. He, L. Zhang and Z. Cheng, *Macromolecules*, 2024, **57**, 756–765.
10 J. Sun, S. Ren, H. Zhao, S. Zhang, X. Xu, L. Zhang and Z. Cheng, *ACS Macro Lett.*, 2023, **12**, 165–171.
11 W. Borzęcka, A. Domiński and M. Kowalczuk, *Nanomaterials*, 2021, **11**, 2426.
12 P. C. Lo, M. S. Rodríguez-Morgade, R. K. Pandey, D. K. P. Ng, T. Torres and F. Dumoulin, *Chem. Soc. Rev.*, 2020, **49**, 1041–1056.

13 A. O. Ribeiro, J. P. C. Tomé, M. G. P. M. S. Neves, A. C. Tomé, J. A. S. Cavaleiro, Y. Iamamoto and T. Torres, *Tetrahedron Lett.*, 2006, **47**, 9177–9180.
14 H. K. Moon, M. Son, J. E. Park, S. M. Yoon, S. H. Lee and H. C. Choi, *NPG Asia Mater.*, 2012, **44**, e12.
15 Y. Yoon, S. Kim and H. Cheul Choi, *NPG Asia Mater.*, 2020, **12**, 16.
16 Z. Wang, S. Gai, C. Wang, G. Yang, C. Zhong, Y. Dai, F. He, D. Yang and P. Yang, *Chem. Eng. J.*, 2019, **361**, 117–128.
17 K. J. Hamam and M. I. Alomari, *Appl. Nanosci.*, 2017, **7**, 261–268.
18 R. Hota, K. Baek, G. Yun, Y. Kim, H. Jung, K. M. Park, E. Yoon, T. Joo, J. Kang, C. G. Park, S. M. Bae, W. S. Ahn and K. Kim, *Chem. Sci.*, 2012, **4**, 339–344.
19 Y. Li, Y. Lian, L. T. Zhang, S. M. Aldousari, H. S. Hedia, S. A. Asiri and W. K. Liu, *Interface Focus*, 2016, **6**, 20150086.
20 C. Nitschke, S. M. O'Flaherty, M. Kröll and W. J. Blau, *J. Phys. Chem. B*, 2004, **108**, 1287–1295.
21 V. V. Nikolaev, M. A. Kaliteevski and N. S. Averkiev, *J. Phys. Chem. C*, 2019, **123**, 27854–27861.
22 K. M. Alam, P. Kumar, S. Gusarov, A. E. Kobryn, A. P. Kalra, S. Zeng, A. Goswami, T. Thundat and K. Shankar, *ACS Appl. Mater. Interfaces*, 2020, **12**, 43992–44006.
23 R. O. Ogbodu and T. Nyokong, *Spectrochim. Acta, Part A*, 2014, **121**, 81–87.
24 X. Hangxun, B. W. Zeiger and K. S. Suslick, *Chem. Soc. Rev.*, 2013, **42**, 2555–2567.
25 B. Naidji, L. Hallez, A. Et Taouil, M. Rebetez and J. Y. Hihn, *Ultrason. Sonochem.*, 2021, **75**, 105610.
26 M. W. Grinstaff and K. S. Suslick, *Proc. Natl. Acad. Sci. U. S. A.*, 1991, **88**, 7708–7710.
27 R. B. d. S. Pinheiro, A. C. d. C. Junior, C. A. T. Zepeda, K. M. P. Ricarte, M. A. Mondragón, O. V. Cabral and C. A. T. Soto, *Rev. Des. Soc.*, 2023, **12**, e18712742678.
28 S. Foley and M. Enescu, *Vib. Spectrosc.*, 2007, **44**, 256–265.
29 M. I. Muñoz, A. J. Aller and D. Littlejohn, *Mater. Chem. Phys.*, 2014, **143**, 1469–1480.
30 D. R. Tackley, G. Dent and W. E. Smith, *Phys. Chem. Chem. Phys.*, 2000, **2**, 3949–3955.
31 T. Kondratenko, O. Ovchinnikov, I. Grevtseva, M. Smirnov, O. Erina, V. Khokhlov, B. Darinsky and E. Tatianina, *Mater*, 2020, **13**, 909.
32 P. Cybulski, M. Bravo, J. J. K. Chen, I. Van Zundert, S. Krzyzowska, F. Taemaitree, H. Uji-i, J. Hofkens, S. Rocha and B. Fortuni, *Front. Cell Dev. Biol.*, 2024, **12**, 1520078.
33 A. Tchoryk, V. Taresco, R. H. Argent, M. Ashford, P. R. Gellert, S. Stolnik, A. Grabowska and M. C. Garnett, *Bioconjug. Chem.*, 2019, **30**, 1371–1384.
34 S. U. Hasnain Bakhtiar, A. Zada, F. Raziq, S. Ali, M. I. Ali Shah, M. Ateeq, M. Khan, D. Alei, P. Fazil, M. Naeem, W. Khan, J. A. Khan, R. Nazir, W. Dong and Q. Fu, *Int. J. Hydrogen Energy*, 2023, **48**, 16320–16329.
35 E. Genc Acar, A. C. Yüzer, G. Kurtay, G. Yanalak, E. Harputlu, E. Aslan, K. Ocakoglu, M. Güllü, M. Ince and I. H. Patir, *ACS Appl. Energy Mater.*, 2021, **4**, 10222–10233.
36 Y. X. Ye, J. Pan, F. Xie, L. Gong, S. Huang, Z. Ke, F. Zhu, J. Xu and G. Ouyang, *Proc. Natl. Acad. Sci. U. S. A.*, 2021, **118**, e2103964118.
37 B. Barrios, B. Mohrhardt, P. V. Doskey and D. Minakata, *Environ. Sci. Technol.*, 2021, **55**, 8054–8067.
38 H. Lee, Y. K. Park, S. J. Kim, B. H. Kim, H. S. Yoon and S. C. Jung, *J. Ind. Eng. Chem.*, 2016, **35**, 205–210.
39 K. Yue, J. Nan, X. Zhang, J. Tang and X. Zhang, *Appl. Therm. Eng.*, 2016, **99**, 1093–1100.
40 Y. Zhu, X. Wang, L. Feng, R. Zhao, C. Yu, Y. Liu, Y. Xie, B. Liu, Y. Zhou and P. Yang, *Nat. Commun.*, 2024, **151**, 8696.
41 W. Zhen, T. Zhao, X. Chen and J. Zhang, *Small*, 2025, **21**, 2500880.